

# PSTM / NSOM modeling by 2-D quadridirectional eigenmode expansion

M. Hammer\*, R. Stoffer

MESA<sup>+</sup> Research Institute, University of Twente, Enschede, The Netherlands

---

**Abstract:** A 2-D model for photon-scanning tunneling microscopy (PSTM) of integrated optical devices is evaluated. The simulations refer to a setup, where the optical field in the vicinity of the sample is probed by detecting the optical power that is transferred via evanescent or radiative coupling to the tapered tip of an optical fiber close to the sample surface. Scanning the tip across the surface leads to a map of the local optical field in the sample. As a step beyond the mere analysis of the sample device, we consider simulations that include the sample as well as the probe tip. An efficient semi-analytical simulation technique based on quadridirectional eigenmode expansions is applied. Results for a series of configurations, where slab waveguides with different types of corrugations serve as samples, allow to assess the relation between the PSTM signal and the local field distribution in the sample. We observed a reasonable qualitative agreement between these computations and a previous experimental PSTM investigation of a waveguide Bragg grating.

**Keywords:** photonics, photon scanning tunneling microscopy, near field scanning optical microscopy, integrated optics, numerical modeling

**PACS codes:** 07.79.Fc 42.82.-m 42.25.Bs

---

## 1 Introduction

Photon scanning tunneling microscopy (PSTM) or near-field scanning optical microscopy (NSOM or SNOM) becomes increasingly popular as a tool to study the local optical electromagnetic field close to the surface of devices from integrated optics / photonics. A typical setup (cf. e.g. Ref. [1]) consists of a tapered tip of an optical fiber, the probe, that is attached to the tuning fork of an atomic-force microscope (AFM). By scanning the probe at a narrow distance, typically a few tens of nanometers, across the sample surface one generates simultaneously a topographical and an optical signal. While in general the optical part of the microscope can be operated in different schemes concerning illumination and detection, here we are interested in setups where the light is fed into the waveguiding sample structure by means of conventional coupling techniques of integrated optics, and where the power detected at the end of the fiber that is attached to the probe tip is recorded as the optical signal.

Examples for these kinds of experiments include the mapping of fields in (multimode) dielectric optical waveguides [2, 3, 4, 5, 6], in an optical Y-junction [7], or in a Mach-Zehnder interferometer [1]. Other studies considered the evolution of optical fields behind a slit-distortion in a waveguide [8], in waveguide Bragg gratings [9], in photonic crystal slabs [10], or in photonic crystal structures with defect cavities [11, 12]. PSTM observations of resonances in cylindrical integrated optical microresonators are reported in Refs. [13, 14, 15].

Besides the actual experiments, simplified microscope models have also been studied by means of numerical simulations, though mostly for different schemes of operation. The optical fields in the surrounding of dielectric (coated or uncoated) or metallic probe tips in two spatial dimensions are investigated in Refs. [16, 17] ([18]: related experiments), [19], and [20]. The simulations include also the interaction of the tip with simple objects on glass substrates: circular dielectric or metallic, nanometer-sized 2-D particles (illumination via the probe), or dipole sources (single molecule fluorescence). Examples for studies in three spatial dimensions are Refs. [21, 22], where the optical field around isolated, metallic or coated dielectric, circular-conical probe tips is considered, or the simulations of the interaction between a conical, uncoated dielectric tip with a freestanding glass bar of nanometer dimensions in Ref. [23]. A variety of computational techniques were applied, including the multiple multipole (MMP) method [24], calculations based on a Greens tensor description [25, 26], or the popular finite-difference time-domain (FDTD) simulations [27, 28].

All previously mentioned numerical investigations focus on the optical field inside and in the immediate vicinity of the probe tip and the simple, nanometer-sized samples. Especially the proper modeling of particular probe shapes is aimed at, with the intention to assess the possibility of sub-wavelength resolution of the microscope,

---

\*Department of Applied Mathematics, University of Twente  
Phone: +31/53/489-3448

Fax: +31/53/489-4833

P.O. Box 217, 7500 AE Enschede, The Netherlands  
E-mail: m.hammer@math.utwente.nl

or to optimize the probe geometry, respectively. In view of the experimental attempts to map the optical fields in the considerably larger photonic structures, however, one would wish to include the entire sample device into the simulation, in order to examine the interaction of the probe tip with the (nontrivial) optical field that establishes in the device under test. An example is the large-scale, full 3-D FDTD study of Ref. [29], where the PSTM observation of optical fields and band structure of a photonic crystal slab has been simulated. Unfortunately, due to the computational complexity of the problem, the 3-D calculations [23, 29] remain restricted to a rather limited computational domain around the actual interaction region, and to a rather limited number of probe/sample configurations.

Hence, for the present contribution we looked at a — highly simplifying — 2-D model of the optical part of the PSTM microscope. Corrugated slab waveguides (cores with slits, short Bragg gratings) serve as samples. A half infinite piece of waveguide, oriented perpendicularly to the axis of the sample structures, represents the probe tip. This model is certainly limited with respect to the range of structures where it can be applied reasonably, and with respect to the aspects of the microscopy technique that can be captured. Nevertheless, efficient 2-D simulation techniques permit to include comparably large sample devices into the calculations, and offer the possibility for detailed studies of the interaction between probe and sample. A recently proposed semianalytical method (quadridirectional eigenmode propagation, QUEP) [30] constitutes a convenient tool for virtual experiments with this model.

After the introduction of the PSTM model, Section 2.1 gives a brief outline of the simulation technique. In Section 3, a series of results for different sample structures are discussed. The examples allow to estimate how the signal detected via the fiber is related to the field intensity at the probe tip, and how the presence of the probe influences the field distribution within the sample. Section 4 compares an experimental PSTM investigation [9] of a waveguide Bragg grating with the results of corresponding 2-D simulations.

## 2 2-D PSTM model

Figure 1(a) introduces the PSTM model. The guided mode of the horizontal slab illuminates the sample from the left with input power  $P_{\text{in}}$ ; the power  $S$  associated with the upwards traveling guided mode of the vertical probe slab represents the primary PSTM signal. A PSTM scan is modeled by evaluating  $S$  as a function of the probe center position  $p$ . Besides  $S$ , the guided transmitted and reflected power fractions  $T$  and  $R$  are recorded to assess in how far the presence of the probe alters the global optical transmission state of the sample.

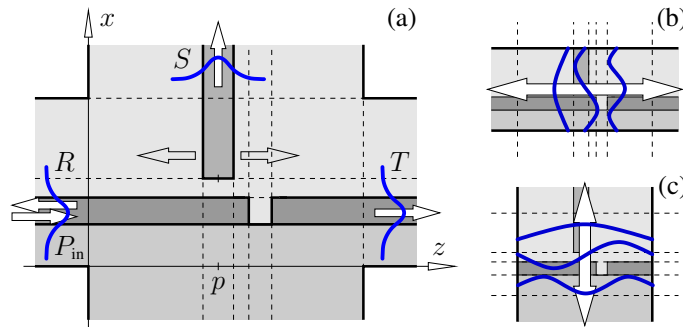


Figure 1: (a): schematic of the 2-D PSTM model, here consisting of a slab waveguide with a hole in the core, the sample, and a half-infinite vertical waveguide segment, the probe. Cartesian coordinates  $x$  and  $z$  denote the horizontal and vertical directions.  $p$  is the  $z$ -position of the probe tip center. The dashed lines indicate the division of the structure into layers and slices, as required for the QUEP simulations. (b, c): QUEP basis fields; the solution of the scattering problem is expanded into eigenmodes of local 1-D multilayer slab profiles that travel along the horizontal (b) and vertical axes (c).

We restrict the discussion to lossless isotropic materials, and consequently to uncoated, purely dielectric probes. For simplicity we also assume that the probe moves along the sample at a constant  $x$ -level, i.e. that the probe does not follow the corrugation of the sample surface. This assumption is reasonable e.g. for the experiments of Ref. [9] (Section 4), where the probe tip diameter is larger than the topological features of the sample.

## 2.1 Simulations by quadridirectional eigenmode propagation

The previous model assumptions lead to 2-D scattering (Helmholtz-) problems with guided in- and outflux, for a purely real, isotropic, and piecewise constant permittivity profile, where all dielectric interfaces are parallel to one of the coordinate axes. The propagation of light with fixed frequency, given by the vacuum wavelength  $\lambda$ , is to be analyzed. Two classes of solutions with definite polarization exist: for TE waves, only the electric field component  $E_y$  perpendicular to the  $x$ - $z$  plane is present (“perpendicular polarization”). In the TM case, the electric field is polarized in the  $x$ - $z$ -plane (“parallel polarization”); then usually the perpendicular magnetic component  $H_y$  is used for a scalar description of the optical field. Note that within the 2-D model, these decoupled, scalar field representations are exact.

The simulation technique as described in detail in Ref. [30] requires to enclose the interesting region in a rectangular window. A solution of the Helmholtz problem is then sought on a cross-shaped computational domain that consists of this interior window, together with the outwards unbounded external stripes that are connected to the four edges. On the four corner points of the inner rectangle and on the boundaries of the external regions, the basic field components ( $E_y$  for TE,  $H_y$  for TM polarization) are assumed to vanish. The bold corners in Figure 1(a) indicate the restriction of the computational domain.

To define the basis fields for the eigenmode expansion, two types of divisions of the computational domain are considered. On the one hand, one views the structure as a sequence of vertical slices (b), such that within each slice the refractive index profile is constant along the  $z$ -axis. The modes associated with these individual slices ( $x$ -dependent profiles, propagation along the  $z$ -axis) constitute one set of basis fields. On the other hand, the structure is decomposed into a stack of horizontal layers (c), where the permittivity is constant along the  $x$ -axis within each layer. The modes associated with the separate layers ( $z$ -dependent profiles, propagation along the  $x$ -axis) form a second set of basis fields. In both cases, the mode spectra are discretized by artificial Dirichlet boundary conditions imposed on the edges of the inner rectangle of the computational domain. Bidirectional versions of propagating and evanescent modes up to certain orders  $M_x$  (related to the division into slices) and  $M_z$  (related to the layer decomposition) are taken into account. Modes traveling in the positive and negative  $x$ - and  $z$ -directions contribute, hence one could call this a “quadrudirectional” eigenmode expansion.

Superpositions of all basis modes establish the ansatz for the optical field, defined piecewise for the individual slices respectively layers. This ansatz satisfies the relevant wave equation everywhere in the computational domain, with the exception of the horizontal and vertical segment boundaries, where the Maxwell equations require certain continuity conditions to be satisfied. Consistent projection of these equalities onto the basis elements (“overlap” computations) with respect to suitable mode products [31, 30] allows to extract a linear system of equations in the so far unknown coefficients of the eigenmode expansion. Assuming that the analytic basis modes are computed exactly, the emerging system of equations permits a stepwise solution. As far as only the segments inside the inner rectangle are concerned, the contributions of the horizontally and vertically propagating modes are decoupled. Conventional bidirectional eigenmode propagation (BEP) schemes [32, 33] can be applied; the present approach is related to the formulation given in [34, 35]. The partial solutions (viewpoints Figure 1(b, c)) are subsequently connected by the equations that belong to the continuity conditions at the four outer edges of the computational rectangle. Only this last (essential) combination step establishes a solution of the wave equation on the entire cross-shaped computational domain.

The optical influx is specified by prescribing the amplitudes of all inwards traveling basis fields on the exterior regions; in the examples of Section 3 typically only one amplitude of the incident guided mode of the horizontal slab is nonzero. This forms a right hand side to the linear system, which is then solved for all remaining expansion coefficients, with the amplitudes of the outgoing basis fields on the exterior stripes as primary unknowns. In Section 3, the optical powers  $S$ ,  $R$ ,  $T$  of the signal, reflected, and transmitted waves can be accessed directly by inspecting the squared coefficients of the outgoing normalized fundamental guided modes related to the upper, left, and right exterior regions.

The QUEP simulations treat the light propagation along both coordinate axes precisely alike. As an alternative to the viewpoint of the cross-shaped computational domain, the perpendicular, dependent superposition of BEP expansions may be viewed as a way to establish *fully transparent boundary conditions* (exception: the corner points) for the inner rectangular computational window, with a straightforward possibility of modeling guided wave influx and outflux. Though somewhat restrictive what concerns the geometrical variability, the technique offers an accurate and quite efficient platform for computational studies of the PSTM model.

### 3 Numerical results

Given a guided wave input into the sample of power  $P_{\text{in}}$ , the squared amplitude of the normalized upwards guided mode of the probe represents the signal  $S$  in our model (usually the major recorded quantity in an actual PSTM experiment; note that for a vertically homogeneous, lossless fiber, the power  $S$  detected at the upper end of the probe does not depend on the length of the waveguide). We observed a predominant expectation that  $S$  should be a measure of the local intensity, i.e. a quantity  $\sim |E_y|^2$  (TE) or  $\sim |H_y|^2$  (TM), at the end of the probe tip. Therefore the plots in the following sections compare curves for  $S/P_{\text{in}}$  and data for  $|E_y|^2(g, p)$  or  $|H_y|^2(g, p)$ , respectively, where  $g$  and  $p$  are the  $x$ - and  $z$ -coordinates of the center of the tip facet. The presence of the probe may change the local intensity, hence two curves for that quantity are given: one set of data points represent a scan along the line  $x = g$  across a solution of the scattering problem without the probe, i.e. the field in the unperturbed sample (replace the  $p$ -axis in the plots by the  $z$ -coordinate). A second curve corresponds to the local intensity in a configuration where the probe tip center is situated at the observation point. Identifiers [s] (sample only) and [s+p] (sample and probe) distinguish these values.

In order to facilitate a quantitative comparison, for each figure the curves [s] and [s+p] for the local intensities have been scaled by a common factor such that the [s]-level coincides with the signal data ( $S$ ) at a single position. Circle symbols mark these scaling points in the corresponding plots. The scaling represents the common procedure to “match” measurements of relative quantities; here the proportionality of the local field [s] and the signal power  $S$  is to be investigated. Naturally, the choice of the scaling points influences to a certain degree the impression given by the plots. We have selected these positions such that the local proportionality between the  $S$  and [s]-curves becomes apparent; none of the conclusions depends on these choices.

All QUEP results shown below have (roughly) been checked for convergence with respect to the extension of the inner computational window, and with respect to the density of the spectral field discretization. Still, for completeness the corresponding data for the computational intervals and for the numbers of basis modes per propagation direction and per slice ( $M_x$ ) or per layer ( $M_z$ ) are given in the captions along with the structural parameters of the computations. Note that the transparent boundary conditions implemented by the QUEP algorithm permit outgoing guided and nonguided waves to leave the inner computational rectangle across the four edges. For the final solution, Dirichlet boundary conditions apply only on the corner points, and on the boundaries of the exterior slices, as indicated in Figure 1(a).

#### 3.1 Probing evanescent fields

An ideal, uncorrugated slab waveguide serves as the first sample. Figure 2 introduces the trial structure. With the exponential decay of the guided slab mode profiles, here the unperturbed fields in the vicinity of the sample structure are known exactly. Hence the slab permits a most straightforward comparison of the PSTM signal with the probed optical field.

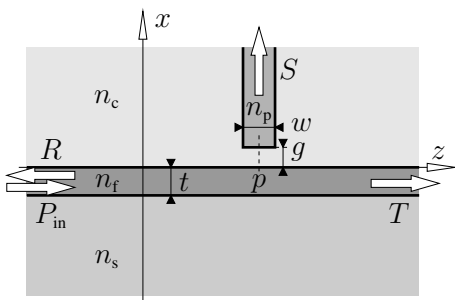


Figure 2: PSTM model configuration. Sample: a slab waveguide, thickness  $t = 0.2 \mu\text{m}$ , refractive indices  $n_s = 1.45$  (substrate),  $n_f = 2.0$  (film),  $n_c = 1.0$  (cladding, background). Probe: a vertical slab, width  $w = 100 \text{ nm}$ , refractive index  $n_p = 1.5$ . Illumination by light with a vacuum wavelength of  $\lambda = 0.633 \mu\text{m}$ . QUEP parameters: computational domain  $(x, z) \in [-3.0, 3.0] \times [-3.0, 3.0] \mu\text{m}^2$ , number of expansion terms  $M_x = M_z = 80$ .

For the  $z$ -invariant sample, the power levels observed for the signal  $S$ , transmission  $T$ , and reflection  $R$  during a horizontal scan at constant height  $g$  should obviously not depend on the probe position  $p$ . This can be used for a consistency check of the simulations: due to the particularities of the spectral discretization one must expect a dependence of the results on the position where the vertical slab is placed inside the computational domain. Reassuringly, for positions where the guided mode profile associated with the probe is contained reasonably within the computational window, we found hardly any variation of  $S$ ,  $T$ , and  $R$  with  $p$  on a scale that becomes relevant for the subsequent configurations with comparable simulation parameters.

For the present parameters, the relative signal levels for TE polarization are by about a factor 4 larger than those for TM waves. A possible explanation could view the perturbation effected by the probe as a dipole source at the probe facet. Its directional radiation pattern includes the probe axis in case the dipole is oriented along the  $y$ -axis, i.e. for TE polarization. For TM polarized light the dipole is oriented in the  $x$ - $z$ -plane more or less along the probe axis, such that the probe receives much less optical power. We therefore restrict most of the following simulations to TE polarized illumination, although, for the present high-contrast structures, one must expect pronounced differences between the polarizations.

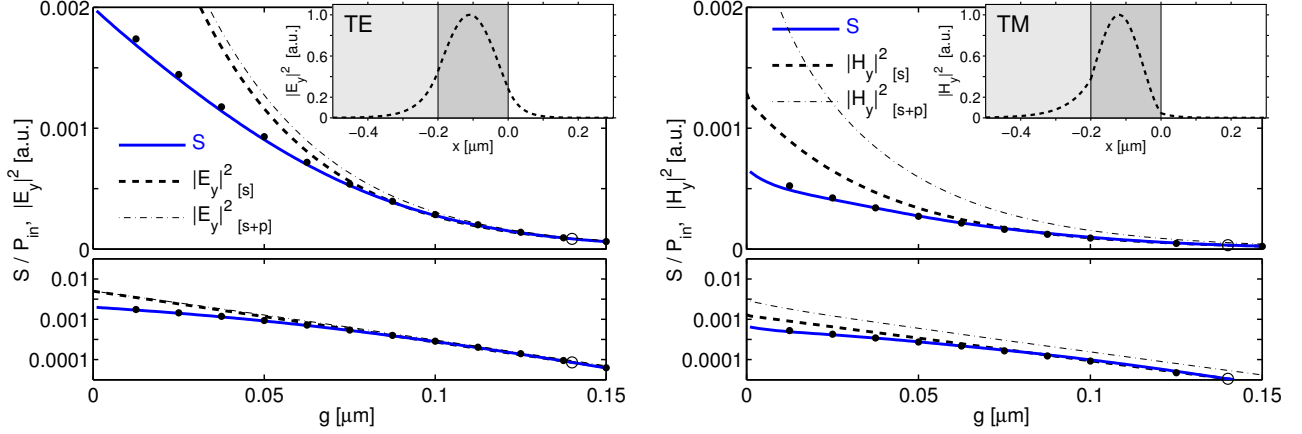


Figure 3: Vertical scan over the slab of Figure 2, for TE- (left) and TM-polarized illumination (right). The curves show the dependence of the PSTM signal  $S$  (continuous) and the local field intensities at the probe tip center  $|E_y|^2$  or  $|H_y|^2$  without the probe ([s], dashed) and with the probe ([s+p], dash-dotted), on the with  $g$  of the gap between probe and sample. FDTD results for the signal (cf. Section 3.1.1) are indicated by filled circular markers. Insets: intensity profiles of the fundamental modes supported by the sample.

A vertical scan turns out to be more interesting. According to corresponding claims based on experimental observations e.g. in Refs. [2, 4, 5, 10, 36], the signal should be proportional to the “intensity at the end of the probe”, here interpreted as the square of the local electromagnetic field that exists at the position of the center of the probe facet, for an absent probe. Hence, if the probe is lifted upwards away from the sample, one expects a purely exponential decay of the signal power with the gap distance  $g$ , according to the exponential shape of the guided mode profile supported by the sample. Figure 3 shows the results of our corresponding calculations.

Contrarily to the expectation, here we can *not* confirm a strict proportionality between the signal and the field intensity at the probe tip. While the squares of the exponential tails of the sample mode profiles are represented by exact straight lines in the logarithmic lower plots of Figure 3, the lines related to the PSTM signal are curved. This holds also for relatively large probe-sample separations, although, according to the plots, for large  $g$  an exponential fit seems to be rather evident.

Most PSTM experiments, however, are operated with a gap between sample and probe of about 10 nanometers. In that regime the proportionality between the signal and the local field intensity in the unperturbed sample is pronouncedly violated. These findings are actually in accordance with an early measurement reported in Ref. [2], where a planar silicon-oxide/silicon-nitride waveguide of thickness 160 nm is considered, illuminated by TE polarized light at a wavelength of 632.8 nm, i.e. a configuration quite similar to Figure 2. Also there a systematic deviation of the PSTM signal from the straight line in the logarithmic plots can be observed, most apparent for small probe-sample separations.

Interestingly, the influence of the probe on the field strength at its tip turns out to be much less pronounced. Figure 3 shows hardly any change between the [s]- and [s+p]-data for TE polarization, and a change by merely an almost constant factor for TM polarized waves. On the scale of the figure the curves for  $|E_y|_{[s+p]}^2$  or  $|H_y|_{[s+p]}^2$  retain the exponential shape of the unperturbed sample field  $|E_y|_{[s]}^2$  or  $|H_y|_{[s]}^2$ , respectively, deviating from the non-exponential behaviour of  $S(p)$ .

In Figure 4 we try to visualize what happens when the probe enters the evanescent field around the sample. Without the probe, only the plane wave fronts of the guided slab modes are visible. If the probe is introduced, as a large-scale effect waves of cylindrical-like shapes appear, originating from the probe tip, with different, material dependent wavelengths in the substrate and cover regions. While the angular distribution is almost symmetrical for TE polarization, the TM waves exhibit a more directional, forward-oriented wave pattern.

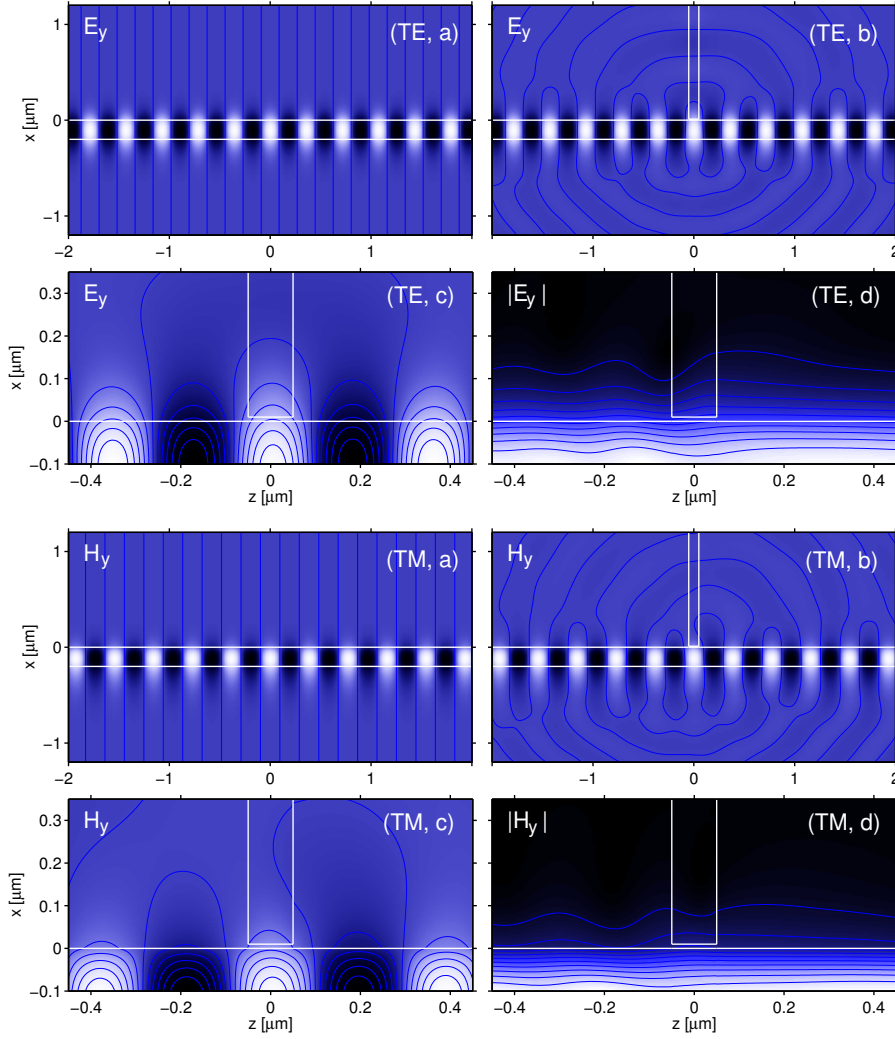


Figure 4: Optical field around the slab waveguide of Figure 2, for TE- (top) and TM-polarized light (bottom). The gray-scale levels correspond to the real, stationary physical fields (a, b, c) (snapshots at an arbitrary time), or to the local absolute value of the principal component (d). (a): the separate sample, (b): sample and probe; the contours indicate the zero level. (c, d): magnification of the region around the probe tip, 11 (c) or 10 (d) equidistant contour lines. The probe-sample distance is  $g = 10$  nm.

Also this difference could be explained by the dipole-source viewpoint mentioned above.

Local field distortions due to the probe are revealed best by the curvature of the contours in the plots of the absolute field values. Without the probe, the contours are straight horizontal lines, spaced according to the mode profile of the  $z$ -homogeneous slab. Apparently some disturbance is necessary to force optical power up the fiber probe. Note that here all effects of the probe relate to rather small fractions of the total incident optical power: for the gap  $g = 10$  nm, the guided relative transmission and reflection evaluate to  $T = 0.994$ ,  $R = 7 \cdot 10^{-5}$  (TE) and  $T = 0.990$ ,  $R = 1 \cdot 10^{-5}$  (TM); only the remaining parts of the power budgets are distributed between the signal and the radiation.

### 3.1.1 Comparison with FDTD results

In order to exclude possible artefacts of the simulation technique, and as an additional check of the somewhat unexpected non-proportionality of the signal and the local field intensity, we verified the above findings by means of an entirely independent numerical method. A rigorous 2-D finite-difference time domain (FDTD) scheme [27, 28, 37] has been applied; below we relate briefly the details of these calculations.

A computational window of  $4.2 \times 4.2 \mu\text{m}^2$  is discretized uniformly by a mesh with step sizes of  $0.0125 \mu\text{m}$ . Perfectly matched layer (PML) boundary conditions enclose the computational domain, with a width of  $0.4 \mu\text{m}$ , a quadratic envelope, and a strength such that the theoretical reflectivity of a wave propagating through the background material at normal incidence is  $10^{-6}$ . The interior of the computational window contains the centered sample waveguide and the probe tip with parameters as given for Figure 2.

Properly polarized modal fields are launched into the sample core using the total field / scattered field approach [28]. Their amplitude is raised according to a half-Gaussian curve with a waist of 10 fs, with the maximum being reached at 40 fs. After this time, the incident field amplitude is kept constant. The simulation runs for a

time of 102.4 fs with a time step of 0.025 fs, until a stationary field is established, after which the overlap with the mode of the probe tip at a distance of  $0.5 \mu\text{m}$  from the top of the calculation window is evaluated. Figure 3 exhibits an excellent agreement between the FDTD and the QUEP results.

What concerns the computational effort, the present QUEP implementation completes the solution of a single scattering problem (one  $g$ -value in Figure 3) in about 6 seconds on an up-to-date PC, using about 4 MB of memory, while our 2-D FDTD program takes about 67 seconds and occupies about 6 MB of memory. Note, however, that the QUEP approach addresses directly the frequency-domain (Helmholtz-) problem that is of interest here, and does not — as is the case with the FDTD — compute an entire time evolution of an optical signal, that is afterwards discarded.

### 3.2 Hole defect in a slab waveguide

As an example for a most simple, localized corrugation, a square hole defect is introduced into the former waveguide sample. Figure 5 specifies the geometry and the relevant parameters. After the basic characterization of the model “tool”, from now on the simulations will be restricted to TE polarized illumination, and to scans with a constant height  $g$ . Figure 6 summarizes the results of a PSTM scan across the hole distortion; Figure 7 shows three examples for the resulting optical field.

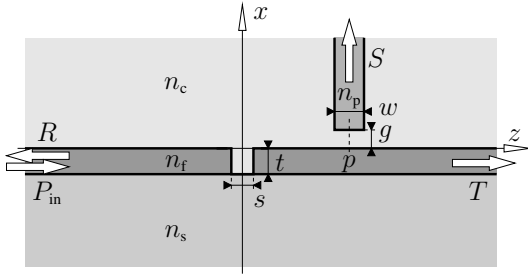


Figure 5: PSTM model configuration. Sample: a slab waveguide with a hole in the core, width  $s = 0.2 \mu\text{m}$ . Other sample and probe parameters are as in Figure 2, with a constant probe-sample distance  $g = 10 \text{ nm}$ . Only TE polarized illumination with a wavelength of  $\lambda = 0.633 \mu\text{m}$  is considered. QUEP parameters:  $(x, z) \in [-3.0, 3.0] \times [-3.1, 3.1] \mu\text{m}^2$ ,  $M_x = M_z = 80$ .

Without the probe, the hole reflects  $R = 19\%$  and transmits  $T = 43\%$  of the incident power; the remaining  $38\%$  are lost to nonguided, radiated fields. The superposition of the unit input and the guided reflection forms partly standing and traveling waves in the input core segment; the confined transmission leads to outwards traveling waves in the ongoing core segment. Both the reflected and transmitted parts of the confined fields undergo a transient oscillation until the lateral shapes of the waves are adapted to the particular profile of the guided mode further away from the defect. The hole acts as a strong localized source, where the radiation consists of waves with cylindrical shapes that originate from the hole, with wavelengths according to the different refractive indices in the substrate and the cover regions.

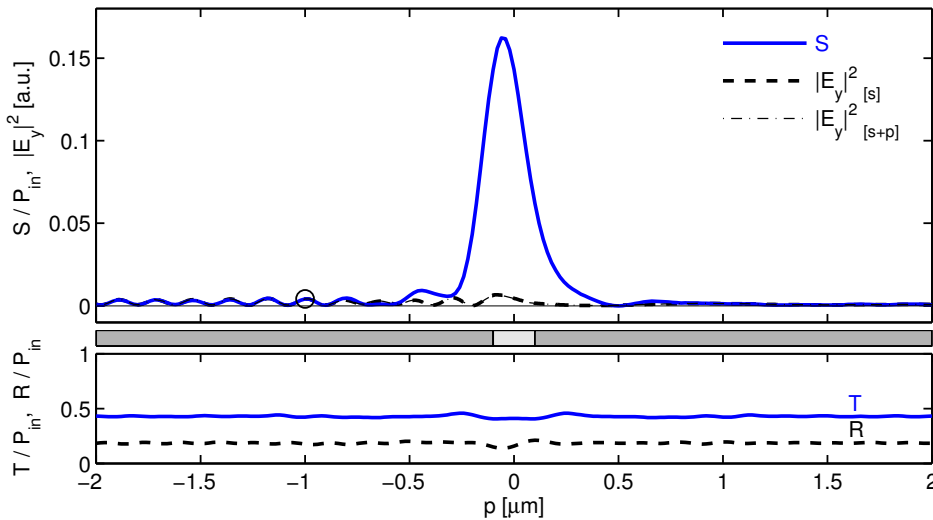


Figure 6: Horizontal PSTM scan across the waveguide defect of Figure 5, signal  $S$  and local field intensity  $|E_y|^2$  (top) versus the  $z$ -position  $p$  of the probe center. Bottom: guided power transmission  $T$  (continuous) and reflection  $R$  (dashed).

If the probe is moved along the sample in a region sufficiently far away ( $|p| \geq 0.7 \mu\text{m}$ ) from the hole, the PSTM signal follows nicely the local intensity of the predominantly evanescent waves that are present in those regions close to the sample surface. The almost periodic intensity pattern of the standing waves can be observed in the input segment. Beyond the hole, the signal corresponds to the lower constant level of the outgoing guided

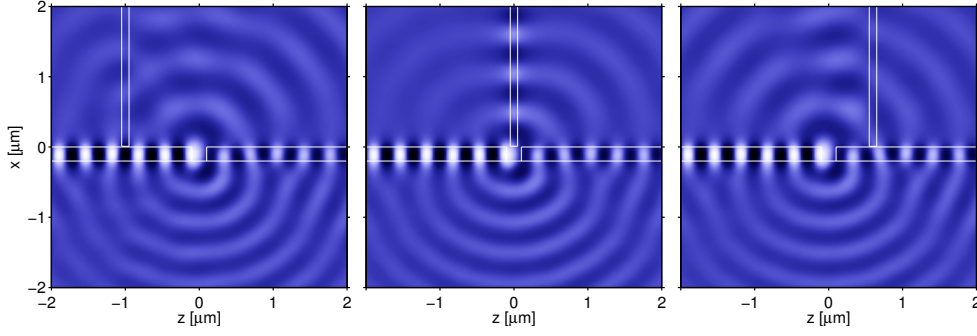


Figure 7: Optical field around the hole in the waveguide of Figure 5, for probes at positions  $p = -1.0, 0.0, 0.6 \mu\text{m}$ . The gray-scales correspond to time snapshots of the stationary physical electric field  $E_y$  of the TE waves.

wave, with a shallow modulation due to the transient adaption to the precise mode profile. The radiated waves from the hole that reach the probe in these regions are partly reflected and transmitted by the vertical slab (cf. the third plot of Figure 7), but do not significantly couple to the upwards traveling mode of the probe, i.e. do not contribute to the signal.

Close to the hole, however, the signal exhibits a strong peak, which obviously must be attributed to direct scattering from the hole upwards into the probe tip. Here the relation between the local field and the signal is entirely lost. With a full width at half maximum of  $0.23 \mu\text{m}$ , the peak is only moderately wider than the defect; the peak maximum is located  $50 \text{ nm}$  to the left of the center of the hole. If the probe is positioned directly above the defect, it collects most of the waves that are otherwise radiated into the upper half space (cf. the middle inset of Figure 7).

### 3.3 Short waveguide Bragg grating

A periodic sequence of holes in a waveguide core forms a waveguide Bragg grating, or “1-D photonic crystal”. Figure 8 introduces a short, deeply etched high-contrast device that shall serve as the next sample. Figures 9 and 10 collect the corresponding results of the PSTM model.

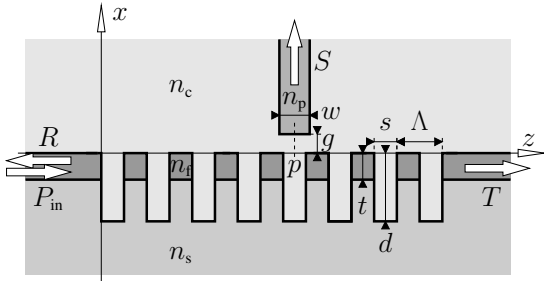


Figure 8: PSTM model configuration. Sample: a short Bragg grating, 8 slits of width  $s = 0.11 \mu\text{m}$ , period  $\Lambda = 0.21 \mu\text{m}$ , and etching depth  $d = 0.6 \mu\text{m}$ . Other sample, probe, and scan parameters are as given for Figures 2, 5. QUEP parameters:  $(x, z) \in [-3.0, 3.0] \times [-3.0, 4.58] \mu\text{m}^2$ ,  $M_x = 100$ ,  $M_z = 120$ .

The geometry of the grating has been adjusted such that it acts as a strong reflector at the given wavelength. Without the probe,  $R = 97\%$  of the input power is reflected, about  $T = 0.1\%$  is transmitted to right-traveling guided modes. The low amount of radiation emanates mainly from the transition from the homogeneous core to the periodically corrugated segment at  $z = 0$ ; Figure 10 shows the interference of these waves with the radiation caused by the probe tip in the substrate and cover regions.

The PSTM signal of Figure 9 remains restricted to the region  $p < 1 \mu\text{m}$  where optical power is actually present in the sample. For positions  $p < -0.5 \mu\text{m}$  before the transition to the grating, the field around the sample consists of interfering forward and backward propagating waves with the same mode profile shape, and is scanned at constant height. Hence the non-proportional effects (Section 3.1) are not relevant here. Just as in Section 3.2, the signal follows the local field intensity at the probe facet.

In the transition region around  $p = 0$ , however, the signal and the sample field intensity deviate considerably. A pronounced peak appears, as before to be attributed to the direct scattering into the probe tip. Here it is accompanied by “sidelobes”, where the signal is actually much lower than the respective sample field intensity; the second but last maximum of the rather regular original standing wave pattern is suppressed almost completely in the signal. Interference effects can obviously also lead to a significant underestimation of the local intensity in the PSTM measurement.

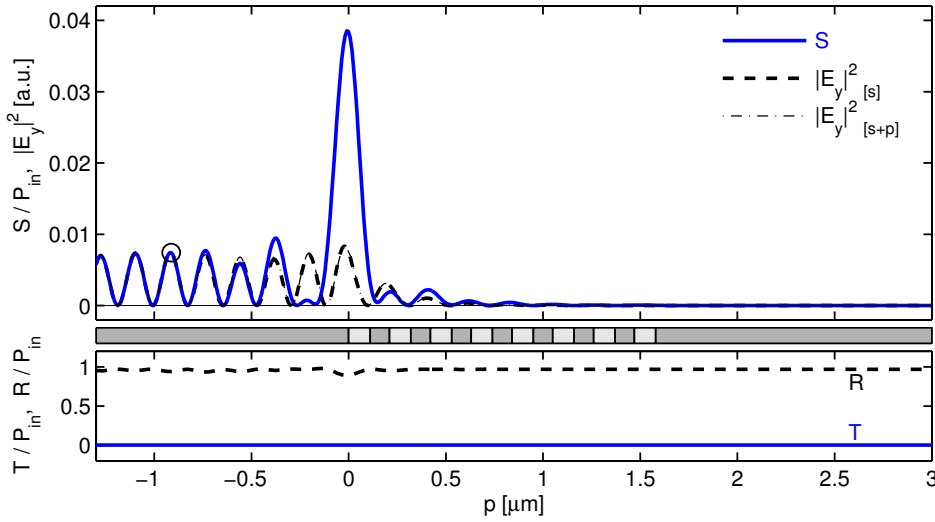


Figure 9: Scan along the Bragg grating of Figure 8; signal  $S$ , local field intensity  $|E_y|^2$ , and transmitted and reflected power  $T$ ,  $R$  as a function of the probe position  $p$ .

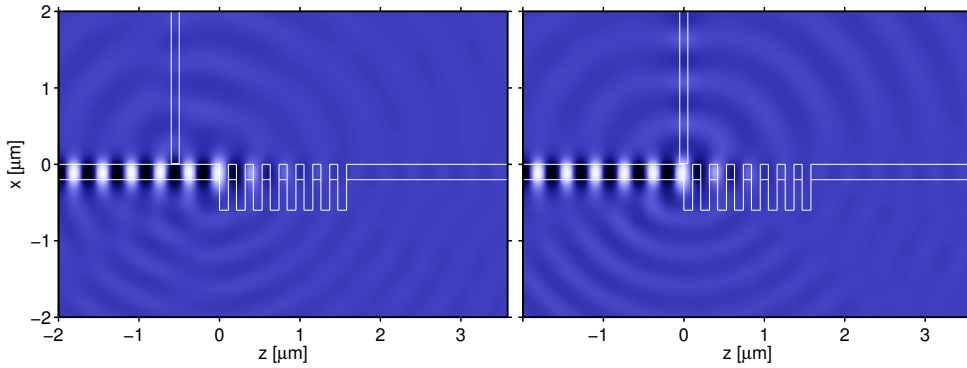


Figure 10: Light propagation through the grating of Figure 8; snapshots of the electric field  $E_y$  for probe positions  $p = -0.55 \mu\text{m}$  and  $p = 0.0 \mu\text{m}$ .

The signal level of 0.04 found at the peak maximum is actually larger than the total amount of power that is lost to radiation if the probe is absent. Apparently, when positioned close to the first discontinuity of the grating the probe does not only collect most of the optical power that is radiated upwards, but it actually raises the level of radiation. The curve  $R(p)$  shows a corresponding dip close to  $p = 0$ , there the guided reflection drops to about 89%. Similar changes of the transmission properties of the sample (rather moderate on the scale of Figures 6, 9) were also observed for the former hole defect. In the following section we consider a structure where the probe interacts with the sample on a much stronger level.

### 3.4 Resonant defect cavity

Introduction of a localized distortion in an otherwise periodic grating can cause drastic changes in the spectral response [38]. Here we realize the defect by enlarging the central “tooth” of the former waveguide Bragg grating. Figure 11 summarizes the geometrical details; Figures 12 and 13 illustrate what happens when the PSTM tip scans across the structure.

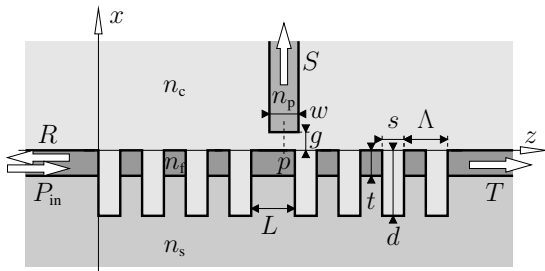


Figure 11: PSTM model configuration. Sample: a short Bragg grating with a central defect, length  $L = 0.2275 \mu\text{m}$ . Other sample, probe, and scan parameters are as given for Figures 2, 5, and 8. QUEP parameters:  $(x, z) \in [-3.0, 3.0] \times [-3.0, 4.7075] \mu\text{m}^2$ ,  $M_x = 100$ ,  $M_z = 120$ .

One may view the device as a sequence of two reflectors, each consisting of a Bragg grating with 4 grooves, that enclose a short homogeneous waveguide segment. The familiar Fabry-Perot model can be applied to explain the occurrence of resonant states within the frequency bandgap of the original long Bragg grating.

The homogeneous section acts as a narrow cavity; resonances manifest as localized transmission peaks in a frequency interval where the device otherwise reflects most of the optical power. The cavity length  $L$  in the specification of Figure 11 has been adjusted such that the defect grating supports a transmission resonance at the vacuum wavelength that will be applied during the PSTM scan.

In its unperturbed state, the structure transmits  $T = 56\%$  and reflects  $R = 6\%$  of the incident power. Radiation originates mainly from the two input and exit transitions between the grating segments and the external homogeneous waveguides, and from the central cavity. The resonance establishes a predominantly standing wave pattern, with two alternating maxima and a central node in the cavity segment, and outwards quickly decaying amplitudes in the grating regions (see the dashed line for  $|E_y|_{[s]}^2$  in Figure 12).

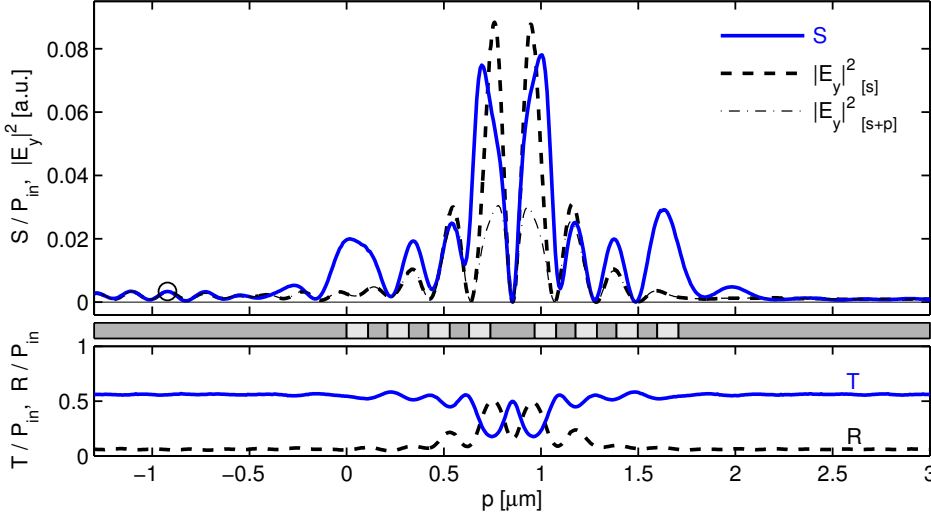


Figure 12: PSTM scan across the defect grating of Figure 11; signal  $S$ , local intensities  $|E_y|^2$ , and the transmission  $T$  and reflection  $R$  effected by the structure, versus the position  $p$  of the probe.

The phenomena identified in the previous examples can be found again in the present PSTM scan: one observes the adequately resolved outer standing wave pattern and the scattering peaks with sidelobes around the transitions to the outer homogeneous segments. Different from the examples in Sections 3.2, 3.3, drastic changes in the transmitted and reflected power levels appear, if the probe scans across the cavity region. The changes in  $T$  and  $R$  are accompanied by a pronounced difference between the  $|E_y|_{[s]}^2$ - and  $|E_y|_{[s+p]}^2$ -curves, i.e. between the field intensity at the position of the tip facet without and with the probe.

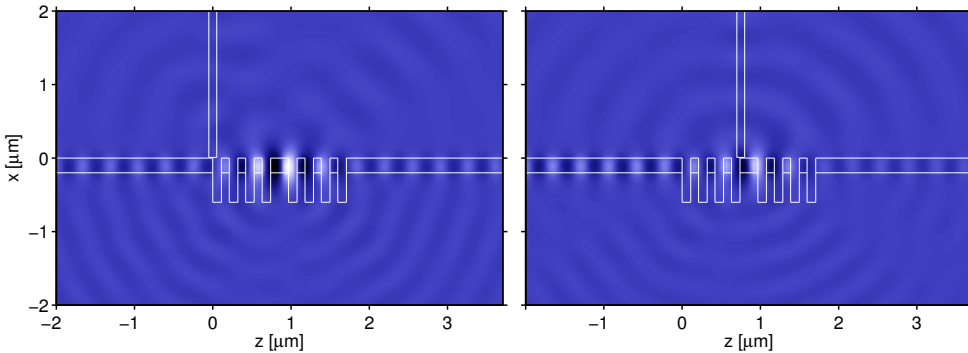


Figure 13: Optical field snapshots for the defect cavity of Figure 11, with the probe located at  $p = 0.0 \mu\text{m}$  (first discontinuity, left) and at  $p = 0.75 \mu\text{m}$  (in the defect region, right). The gray-scale levels of the plots are comparable.

Obviously here the probe effects a major change of the global optical state in the sample, i.e. causes a breakdown of the resonance. Extremal levels of  $T = 0.18$  and  $R = 0.50$  are reached for  $p = 0.75 \mu\text{m}$ . The field in the sample experiences the strongest influence if the probe is positioned close to one of the two maxima of the unperturbed resonant field pattern. The raised reflection is clearly visible in the second inset of Figure 13 as the larger strength of the standing wave pattern. Somewhat surprisingly, the signal recorded for the cavity region is not too far off from the local intensity in the unperturbed sample. Apparently the contribution of the scattering to the signal compensates for the decay of the local intensity due to the resonance breakdown.

The precisely opposite effect can be achieved in a structure with slightly modified cavity length  $L = 0.224 \mu\text{m}$ . For absent probe, this specifies an off-resonance configuration at the operation wavelength, with a rather high reflection  $R = 0.70$  and lower transmission level  $T = 0.15$ . During the scan along the defect, one observes again pronounced variations in  $T$ ,  $R$ , and in the local field intensity, now with the roles of  $T$  and  $R$  reversed

when compared to Figure 13. Around the position  $p = 0.75 \mu\text{m}$  the extremal values of  $R = 0.30$  and  $T = 0.24$  are found. Here the probe shifts the system towards a resonance that does not occur in the isolated sample device.

## 4 Bragg grating: experimental results

A waveguide Bragg grating is investigated in an actual experiment in Ref. [9]. The sample consists of a shallow rib waveguide with a  $\text{Si}_3\text{N}_4$  core, supported by a relatively thick  $\text{SiO}_2$  buffer layer on a Silicon substrate. A series of wide, deeply etched rectangular slits forms the grating. Figure 14 introduces schematically the experimental parameters that are relevant for the present discussion.

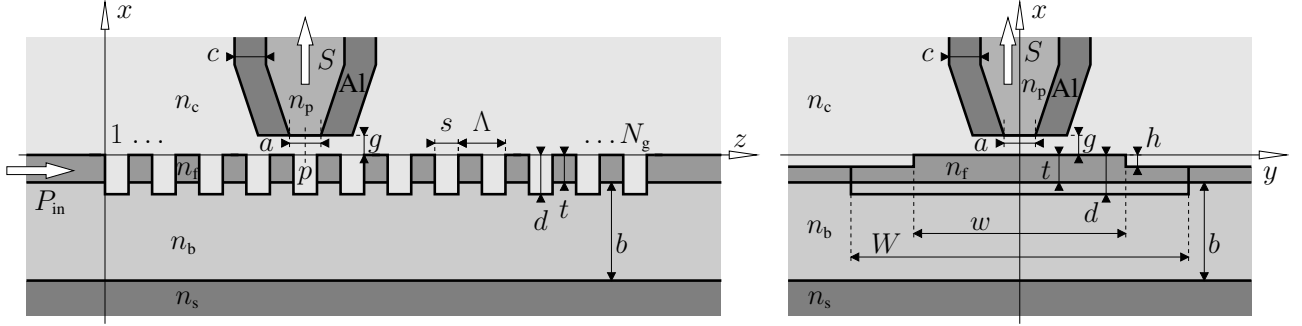


Figure 14: Schematic of an experimental PSTM configuration [9], cross section views of planes parallel (left) and perpendicular (right) to the waveguide axis. Sample: a rib waveguide with a series of rectangular slits, with refractive indices  $n_s = 3.4$  (substrate),  $n_b = 1.45$  (buffer),  $n_f = 2.01$  (core),  $n_c = 1.0$  (cover), film thickness  $t = 55 \text{ nm}$ , rib etching depth  $h = 11 \text{ nm}$ , rib width  $w = 1.5 \mu\text{m}$ , transverse slit width  $W = 2.5 \mu\text{m}$ , buffer layer thickness  $b = 3.2 \mu\text{m}$ , grating period  $\Lambda = 220 \text{ nm}$ , longitudinal slit width  $s = 110 \text{ nm}$ , slit etching depth  $d = 70 \text{ nm}$ , number of grooves  $N_g = 15$ . Probe: a tapered cylindrical fiber tip with aluminium coating, aperture diameter  $a \approx 80 \text{ nm}$ , cladding thickness  $c \approx 100 \text{ nm}$ , core refractive index  $n_p = 1.5$ , distance probe / rib surface  $g = 10 \text{ nm}$ . The Bragg grating is illuminated by TE ( $y$ -) polarized light with a vacuum wavelength  $\lambda = 0.6328 \mu\text{m}$ .

For the PSTM observation the sample is illuminated via end-facet coupling through a microscope objective. By using the feedback from the AFM signal, the optical probe is raster-scanned at a constant distance across the surface of the rib waveguide. Since the diameter of the probe facet (including the coating) is larger than the slit width, at least for probe positions above the actual rib one can assume a constant scan height. One obtains a “top view” PSTM image of the optical field above the sample structure, together with the topological information that allows to precisely relate the optical data to the positions on the sample. Figure 15 shows a section of the 2-D PSTM image along the axis of the sample waveguide. See Ref. [9] for further details concerning the experimental setup and the full measurement results.

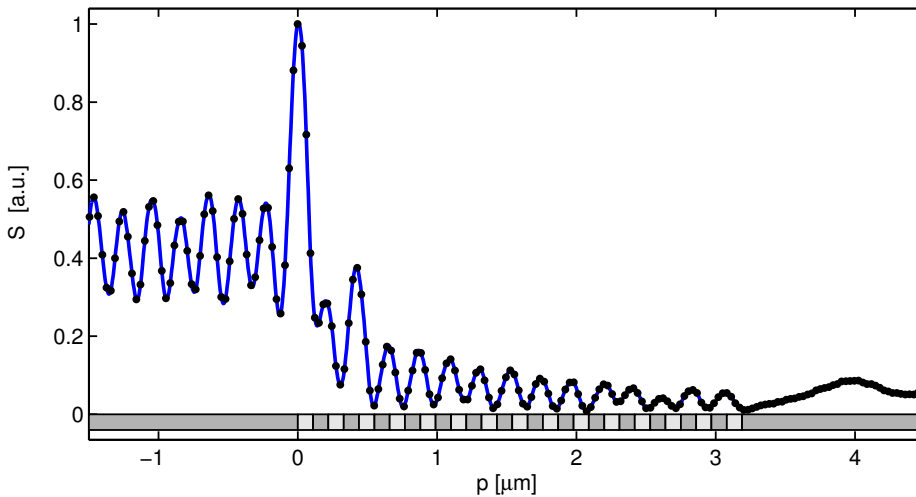


Figure 15: PSTM scan along the center of the corrugated rib of Figure 14, signal power  $S$  depending on the  $z$ -position  $p$  of the probe; experimental data from Ref. [9].

## 4.1 2-D QUEP model

Due to the wide, weak lateral features of the Bragg grating one can expect that the optical field also varies only slowly along the  $y$  direction, when compared with the longitudinal wavelength. We therefore take a cross section along the waveguide axis as the basis for the definition of the sample in our 2-D simulations. This leads to the model geometry of Figure 16. While the buffer layer is of sufficient thickness to prevent leakage of the guided fields into the substrate, it can not a priori be excluded that reflections of scattered waves from the substrate contribute to the PSTM signal. Therefore the substrate / buffer layer interface is included in the simulations (though not the strong material attenuation of the Silicon). Figures 17, 18 show the corresponding results of the model.

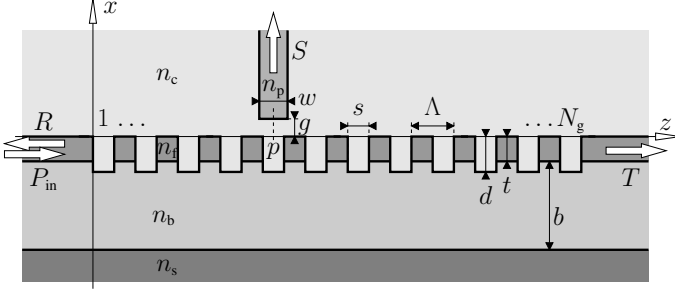


Figure 16: 2-D model of the 3-D configuration in Figure 14. Parameters, sample:  $n_s = 3.4$ ,  $n_b = 1.45$ ,  $n_f = 2.01$ ,  $n_c = 1.0$ ,  $t = 55$  nm,  $b = 3.2$   $\mu\text{m}$ ,  $d = 70$  nm,  $\Lambda = 220$  nm,  $s = 110$  nm,  $N_g = 15$ ; probe:  $w = 100$  nm,  $n_p = 1.5$ ;  $g = 10$  nm, TE,  $\lambda = 0.6328$   $\mu\text{m}$ . QUEP parameters:  $(x, z) \in [-3.5, 1.5] \times [-2.0, 5.2]$   $\mu\text{m}^2$ ,  $M_x = 80$ ,  $M_z = 100$ .

With the small film thickness, the waveguide operates under conditions very close to cut-off. As a consequence, a large fraction of the modal profile stretches out into the buffer region below  $x = -70$  nm, where those fields do not encounter the slits directly. Therefore the grating constitutes only a moderate reflector at the given wavelength. The 2-D simulations predict a guided transmission of  $T = 42\%$  and a reflection of only  $R = 9\%$ . According to Figure 18, when entering the corrugated region, the major part of the light waves forms of a strong beam that propagates at a shallow angle underneath the slits. Beyond the grating, a fraction of that power “leaks” back into the ongoing guided mode. Together with waves that are reflected from the buffer layer / substrate interface, the transient field adaption to the profile of the transmitted guided mode establishes a recovery pattern with a particular scheme of local minima (not shown in Figure 18). Details of the experimental observation of this pattern are discussed in Ref. [9].

For the separate sample structure, Figure 17 indicates that the field intensity  $|E_y|_{[s]}^2$  above the slits drops from the initially large level at the entrance to the grating to quite small values at the exit, where the exit value is much lower than the level that corresponds to the large overall transmission. The decay, and the subsequent recovery of the local intensity, can also be explained by the gradual displacement of the beam center towards the substrate, and by the back-flow of the waves into the core afterwards.

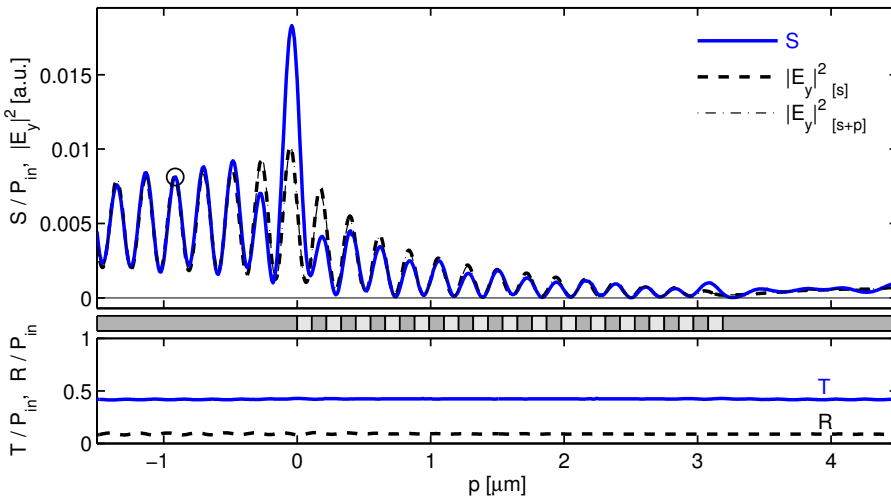


Figure 17: PSTM scan along the waveguide Bragg grating of Figure 16, 2-D model results for Figure 15. Signal  $S$ , local field intensities  $|E_y|^2$ , and guided transmission  $T$  and reflection  $R$  versus the probe position  $p$ .

We find a good qualitative agreement of the simulations in Figure 17 with the experimental data of Figure 15. In the experiment as well as in the model, the PSTM signals map adequately the standing wave pattern in front of the sample, the decay in the grating region, and the recovery process after the end of the grating. Since these

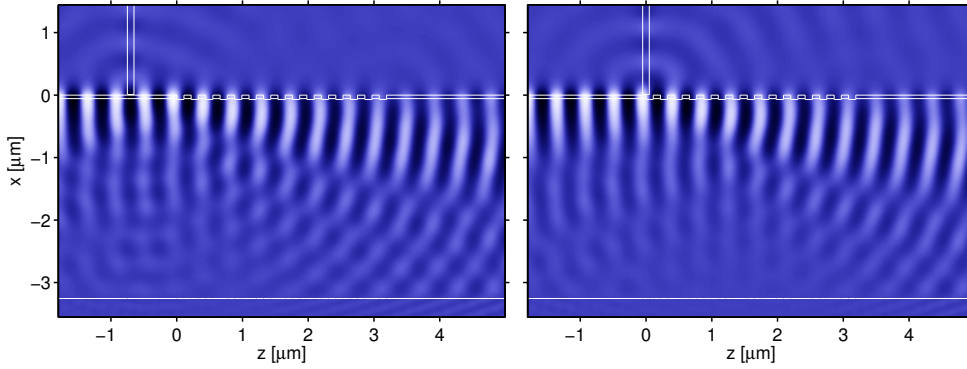


Figure 18: Snapshots of the optical electric field according to the 2-D Bragg grating model of Figure 16, for probe positions  $p = -0.7 \mu\text{m}$  (left) and  $p = 0.0 \mu\text{m}$  (right, beginning of the grating).

features are indeed present in the  $|E_y|_{[s]}^2$ -curve of the model, one can expect that also the field intensity in the real device has a similar shape in the respective regions. Around the input transitions, however, the simulated PSTM signal does not follow the much more regular local field intensity. Since the large scattering peak and the partial suppression of the adjacent maxima occur in the experimental data as well, the model clearly identifies these features as artefacts of the PSTM observation (cf. the corresponding remarks in Ref. [9]).

Although the approximation of an only weak lateral confinement of the optical field in the 3-D sample is very plausible, the experimental probe has a circular aperture, which implies a strong localization of the upwards traveling signal waves. Also other experimental circumstances like the effects of the aluminium coating are not incorporated into the model, hence one can hardly expect a better quantitative agreement between Figures 15 and 17. Note, however, that the scattering peak as predicted here for the uncoated model probe appears in the experimental data as well. If one interpretes the peak as a consequence of direct scattering into the probe aperture, the aluminium coating does obviously not suppress that effect.

## 5 Concluding remarks

Based on a semianalytical quadridirectional eigenmode expansion technique (QUEP), a series of virtual experiments in the framework of a simple 2-D PSTM model have been carried out. We adopted typical parameters for high contrast, single-mode slab waveguides in the  $\text{SiO}_2 / \text{Si}_3\text{N}_4$  material system. The simulations led to the following observations.

Even in cases where a purely evanescent field surrounds the sample, e.g. for a guided mode traveling along an ideal waveguide core, the PSTM signal is not strictly proportional to the local field intensity, if the dependence on the probe-sample distance is considered. Single distortions in the sample surface, or abrupt discontinuities between different homogeneous or periodic sample segments, act as localized sources that can cause pronounced direct scattering into the probe. At these probe locations the signal exhibits strong peaks that are not present in the local intensity of the sample field. Around the peaks, interference effects can lead to an underestimation of the sample intensity by the PSTM signal. If the sample supports resonant states, the presence of the probe can cause a breakdown of an existing resonance, or the build-up of an otherwise nonexistent one. In these cases the probe changes significantly the global optical state of the sample. Unfortunately, all these effects occur where a precise field measurement would be most interesting.

With the exception of these resonant configurations, for TE polarized light we found systematically only very minor changes in the local field strength at the tip position due to the presence of the probe. In the TM case, however, the example of the uncorrugated slab showed that the changes in the local intensity at the tip end can be much more pronounced. These observations should be of relevance for PSTM experiments that rely on the local density of states at the tip of the probe, e.g. for attempts to detect fluorescence properties of single molecules [20, 39]. For specific configurations, where a purely evanescent sample field consists of guided modes with identical profile shapes, and where the probe is kept at constant height above the sample, a reasonable recording of the optical wave patterns in the sample is possible, e.g. the observation of periods of (partially) standing waves. Despite the simplicity of the model, we found an ample qualitative agreement of these simulations with real PSTM experiments on a waveguide Bragg grating.

A number of modifications of the measurement technique can easily be modeled with the present tools. On the one hand this concerns different schemes of illumination and detection: a localized illumination via the probe, with the transmission through the sample detected as the signal [40], alternatively a nonlocal illumination of the sample by a focused external beam, with the light collected by the probe, on a side opposite to the illumination, as the signal [11]. On the other hand, different modes of signal recording could be considered: by evaluating the interference with a reference wave, phase maps of the local electromagnetic field around the sample can be generated [41, 6, 36]. In all cases, a numerical assessment of the microscopy techniques within the present model should be straightforward.

Concerning the question in how far an experimental PSTM signal can be regarded as a quantitative “map” of the “optical field” in the device under test, we could point out several configurations where, according to the model, this simple notion definitely fails. Either the proportionality between the PSTM signal and the local intensity is entirely lost, or, even worse, the presence of the probe influences significantly the optical state of the sample. In fact, we could confirm an approximate proportionality exclusively for the constant-height scans along configurations with local single-mode standing wave patterns. Disturbance effects must be expected e.g. in any PSTM observations of high-quality resonances in photonic micro- and nano-cavities, in principle. While one should certainly be aware of these findings when executing PSTM measurements on photonic structures, we do not think it adequate, however, to attempt, only on the basis of the simplifying 2-D model, any more general quantitative characterization of experimental settings where these artefacts occur, or where they can be excluded.

## Acknowledgments

*The authors thank E. van Groesen and H. J. W. M. Hoekstra for fruitful discussions about the numerical simulations, and E. Flück, L. Kuipers, and N. F. van Hulst for valuable information about the details of the PSTM experiments. E. Flück kindly provided the experimental data for Figure 15.*

## References

- [1] M. L. M. Balistreri, J. P. Korterik, G. J. Veldhuis, L. Kuipers, and N. F. van Hulst. Quantitative photon tunneling and shear-force microscopy of planar waveguide splitters and mixers. *Journal of Applied Physics*, 89(6):3307–3314, 2001.
- [2] D. P. Tsai, H. E. Jackson, R. C. Reddick, S. H. Sharp, and R. J. Warmack. Photon scanning tunneling microscope study of optical waveguides. *Applied Physics Letters*, 56(16):1515–1517, 1990.
- [3] C. D. Poweleit, D. H. Naghski, S. M. Lindsay, J. T. Boyd, and H. E. Jackson. Near-field scanning optical microscopy measurements of optical intensity distributions in semiconductor channel waveguides. *Applied Physics Letters*, 69(23):3471–3473, 1996.
- [4] G. H. Vander Rhodes, B. B. Goldberg, M. S. Ünlü, S. T. Chu, W. Pan, T. Kaneko, Y. Kokobun, and B. E. Little. Measurement of internal spatial modes and local propagation properties in optical waveguides. *Applied Physics Letters*, 75(16):2368–2370, 1999.
- [5] M. L. M. Balistreri, J. P. Korterik, L. Kuipers, and N. F. van Hulst. Photon scanning tunneling microscopy with a three-dimensional multiheight imaging mode. *Applied Physics Letters*, 77(25):4092–4094, 2000.
- [6] M. L. M. Balistreri, J. P. Korterik, L. Kuipers, and N. F. van Hulst. Phase mapping of optical fields in integrated optical waveguide structures. *Journal of Lightwave Technology*, 19(8):1169–1176, 2001.
- [7] M. L. M. Balistreri, J. P. Korterik, L. Kuipers, and N. F. van Hulst. Visualization of mode transformation in a planar waveguide splitter by near-field optical phase imaging. *Applied Physics Letters*, 79(7):910–912, 2001.
- [8] C. Peeters, E. Flück, A. M. Otter, M. L. M. Balistreri, J. P. Korterik, L. Kuipers, and N. F. van Hulst. Photon scanning tunneling microscopy of tailor-made photonic structures. *Applied Physics Letters*, 77(1):142–144, 2000.
- [9] E. Flück, M. Hammer, A. M. Otter, J. P. Korterik, L. Kuipers, and N. F. van Hulst. Amplitude and phase evolution of optical fields inside periodic photonic structures. *Journal of Lightwave Technology*, 21(5):1384–1393, 2003.
- [10] A. L. Campillo, J. W. P. Hsu, C. A. White, and A. Rosenberg. Mapping the optical intensity distribution in photonic crystals using a near-field scanning optical microscope. *Journal of Applied Physics*, 89(5):2801–2807, 2001.

- [11] P. Kramper, A. Birner, M. Agio, C. M. Soukoulis, F. Müller, U. Gösele, J. Mlynek, and V. Sandoghdar. Direct spectroscopy of a deep two-dimensional photonic crystal microresonator. *Physical Review B*, 64:233102, 2001.
- [12] K. Okamoto, M. Lončar, T. Yoshie, A. Scherer, Y. Qui, and P. Gogna. Near-field scanning optical microscopy of photonic crystal nanocavities. *Applied Physics Letters*, 82(11):1676–1678, 2003.
- [13] D. J. W. Klunder, M. L. M. Balistreri, F. C. Blom, H. J. W. M. Hoekstra, A. Driessen, L. Kuipers, and N. F. van Hulst. High-resolution photon-scanning tunneling microscope measurements of the whispering gallery modes in a cylindrical microresonator. *IEEE Photonics Technology Letters*, 12(11):1531–1533, 2000.
- [14] M. L. M. Balistreri, D. J. W. Klunder, F. C. Blom, A. Driessen, J. P. Korterik, L. Kuipers, and N. F. van Hulst. Experimental analysis of the whispering-gallery modes in a cylindrical optical microcavity. *Journal of the Optical Society of America B*, 18(4):465–471, 2001.
- [15] D. J. W. Klunder, M. L. M. Balistreri, F. C. Blom, H. J. W. M. Hoekstra, A. Driessen, L. Kuipers, and N. F. van Hulst. Detailed analysis of the intracavity phenomena inside a cylindrical microresonator. *Journal of Lightwave Technology*, 20(3):519–529, 2002.
- [16] L. Novotny, D. W. Pohl, and P. Regli. Light propagation through nanometer-sized structures: the two-dimensional-aperture scanning near-field optical microscope. *Journal of the Optical Society of America A*, 11(6):1768–1779, 1994.
- [17] L. Novotny, D. W. Pohl, and P. Regli. Near-field, far-field and imaging properties of the 2-D aperture SNOM. *Ultramicroscopy*, 57:180–188, 1995.
- [18] B. Hecht, D. W. Pohl, H. Heinzelmann, and L. Novotny. “Tunnel” near-field optical microscopy: TNOM-2. *Ultramicroscopy*, 61:99–104, 1995.
- [19] A. Castiaux, A. Dereux, J.-P. Vigneron, C. Girard, and O. J. F. Martin. Electromagnetic fields in two-dimensional models of near-field optical microscope tips. *Ultramicroscopy*, 60:1–9, 1995.
- [20] R. X. Bian, R. C. Dunn, and X. S. Xie. Single molecule emission characteristics in near-field microscopy. *Physical Review Letters*, 75(26):4772–4775, 1995.
- [21] L. Novotny, D. W. Pohl, and B. Hecht. Scanning near-field optical probe with ultrasmall spot size. *Optics Letters*, 20(9):970–972, 1995.
- [22] L. Novotny, R. X. Brian, and X. S. Xie. Theory of nanometric optical tweezers. *Physical Review Letters*, 79(4):645–648, 1997.
- [23] G. von Freymann, Th. Schimmel, M. Wegener, B. Hanewinkel, A. Knorr, and S. W. Koch. Computer simulations on near-field optical microscopy: Can subwavelength resolution be obtained using uncoated optical fiber probes? *Applied Physics Letters*, 73(9):1170–1172, 1998.
- [24] Ch. Hafner. *The Generalized Multipole Technique for Computational Electromagnetics*. Artech House, Boston, USA, 1990.
- [25] O. J. F. Martin, A. Dereux, and C. Girard. Iterative scheme for computing exactly the total field propagating in dielectric structures of arbitrary shape. *Journal of the Optical Society of America A*, 11(3):1073–1080, 1994.
- [26] O. J. F. Martin, C. Girard, and A. Dereux. Generalized field propagator for electromagnetic scattering and light confinement. *Physical Review Letters*, 74(4):526–529, 1995.
- [27] K. S. Yee. Numerical solution of boundary value problems involving Maxwell’s equations in isotropic media. *IEEE Transactions on Antennas and Propagation*, 14(3):302–307, 1966.
- [28] A. Taflove. *Computational Electrodynamics: The Finite Difference Time Domain Method*. Artech House Inc., Norwood, MA, USA, 1995.
- [29] S. Fan, I. Appelbaum, and J. D. Joannopoulos. Near-field scanning optical microscopy as a simultaneous probe of fields and band structure of photonic crystals: A computational study. *Applied Physics Letters*, 75(22):3461–3463, 1999.
- [30] M. Hammer. Quadridirectional eigenmode expansion scheme for 2-D modeling of wave propagation in integrated optics. *Optics Communications*, 235(4–6):285–303, 2004.
- [31] C. Vassallo. *Optical Waveguide Concepts*. Elsevier, Amsterdam, 1991.
- [32] G. Sztefka and H. P. Nolting. Bidirectional eigenmode propagation for large refractive index steps. *IEEE Photonics Technology Letters*, 5(5):554–557, 1993.
- [33] J. Willems, J. Haes, and R. Baets. The bidirectional mode expansion method for two-dimensional waveguides: the TM case. *Optical and Quantum Electronics*, 27:995–1007, 1995.

- [34] M. Lohmeyer and R. Stoffer. Integrated optical cross strip polarizer concept. *Optical and Quantum Electronics*, 33(4/5):413–431, 2001.
- [35] M. Lohmeyer. Mode expansion modeling of rectangular integrated optical microresonators. *Optical and Quantum Electronics*, 34(5):541–557, 2002.
- [36] A. L. Campillo and J. W. P. Hsu. Intensity and phase mapping of guided light in LiNbO<sub>3</sub> waveguides with an interferometric near-field scanning optical microscope. *Applied Optics*, 42(36):7149–7156, 2003.
- [37] R. Stoffer, H. J. W. M. Hoekstra, R. M. de Ridder, E. van Groesen, and F. P. H. van Beckum. Numerical studies of 2D photonic crystals: Waveguides, coupling between waveguides and filters. *Optical and Quantum Electronics*, 32:947–961, 2000.
- [38] A. Suryanto, E. van Groesen, M. Hammer, and H. J. W. M. Hoekstra. A finite element scheme to study the nonlinear optical response of a finite grating without and with defect. *Optical and Quantum Electronics*, 35(4):313–332, 2003.
- [39] N. F. van Hulst, J.-A. Veerman, M. F. García-Parajó, and L. Kuipers. Analysis of individual (macro)molecules and proteins using near-field optics. *Journal of Chemical Physics*, 112(18):7799–7810, 2000.
- [40] E. Flück, N. F. van Hulst, W. L. Vos, and L. Kuipers. Near-field investigation of three-dimensional photonic crystals. *Physical Review E*, 68:015601(R), 2003.
- [41] M. L. M. Balistreri, J. P. Korterik, L. Kuipers, and N. F. van Hulst. Local observations of phase singularities in optical fields in waveguide structures. *Physical Review Letters*, 85(2):294–297, 2000.